Micromechanical modelling of edge failure in 800 MPa advanced high strength steels

N. Pathak, C. Butcher, J. Adrien, E. Maire, M. Worswick

Micromechanical modelling of edge failure in 800 MPa advanced high strength steels

N. Pathak[a,*], C. Butcher[a], J. Adrien[b], E. Maire[b], M. Worswick[a]

[a] *Department of Mechanical and Mechatronics Engineering, University of Waterloo, Waterloo, ON, Canada*
[b] *GEMPPM, INSA de Lyon, Lyon, Villeurbanne, France*

ARTICLE INFO

Article history:
Received 6 December 2018
Revised 3 October 2019
Accepted 26 December 2019
Available online 26 December 2019

Keywords:
Ductile failure
Sheared edge stretching
Damage-based fracture model
AHSS

ABSTRACT

Sheared edge failure is one of the major problems associated with the forming of advanced high strength steels (AHSS) such as dual-phase (DP) steels. To improve the performance of AHSS in industrial forming operations, ferritic-bainitic complex-phase (CP) steels have been developed and are gaining attention in academia as well as industry. The present work aims to investigate the influence of microstructure on micro-void (damage) evolution during the edge stretching of CP800 and DP780 steels and develop a micromechanics-based fracture model to predict edge failure for both reamed and sheared holes. Three-dimensional damage histories were obtained using x-ray microtomography on a series of hole tension specimens interrupted at different strain levels. These experiments considered a tensile specimen with a sheared hole at the center of specimen (sheared edge condition) or reamed (ideal edge condition). Void damage measurements, such as void area fraction, number of voids, void diameter, and void aspect ratio, were conducted and the results are compared to the reamed specimens to isolate the sheared edge effect on damage. The void measurements were used to implement a stress-state dependent model for nucleation, and coupled with the Ragab (2004) model for void growth and the Benzerga and Leblond (2014) model for void coalescence to develop a damage-based material model. Higher damage accumulation was observed behind the sheared edge in comparison the reamed edge at a given strain for both materials considered. An uncoupled anisotropic damage-based fracture model was formulated in a LS-DYNA user-defined material subroutine. As an alternative to computationally expensive multi-stage sheared edge stretching simulations, the measured strain-distribution of the sheared edge was mapped into a finite-element model to predict sheared edge failure. The proposed model was validated for the hole tension testing simulations and found to predict failure accurately for both the CP800 and DP780 for both the edge conditions.

1. Introduction

Advanced high strength steels (AHSS) generally offer high strength and moderate formability, however, challenges exist in the application of AHSS including fracture of previously sheared edges during forming operations (Dykeman et al., 2011).

* Corresponding author.
E-mail address: n3pathak@uwaterloo.ca (N. Pathak).

The shearing process generates work-hardening and introduces pre-nucleated voids (damage) due to the high strength-differential between the phases in dual-phase (DP) steels; as a result, a severe residual strain field is generated that accelerates the fracture mechanism of void nucleation, growth and coalescence during hole expansion (Pathak et al., 2017). In order to support application of AHSS in the design of lightweight structures, there is a need to develop fracture models that can predict failure during sheared edge stretching in metal forming simulations.

Extensive literature is available with a focus on modeling the three stages of ductile fracture: nucleation, growth and coalescence of microvoids (Worswick and Pick, 1990; Thomason et al., 1998; Pardoen and Hutchinson, 2000; Landron et al., 2011; Scheyvaerts et al., 2011). Gurson (1977) proposed a porous yield function to account for the effect of void growth and nucleation on the material response. Chu and Needleman (1980) extended this nucleation model to assume that the nucleation rate can be expressed in terms of a normal distribution about a mean nucleation stress or strain. The plastic strain-based variant of the Chu and Needleman (1980) nucleation model has become widely adopted due to its ease of implementation in finite-element codes relative to the stress-based criterion. Tvergaard and Needleman (1984) proposed a coalescence criterion that identifies the onset of coalescence based on critical porosity. Becker (1987) and Koplik and Needleman (1988) reported influence of the material, stress-states and hardening on failure porosities. Subsequently, the Thomason (1999) plastic limit-load model has greatly contributed to the understanding and modeling of void coalescence and has been validated and enhanced by many researchers (Benzerga, 2002; Scheyvaerts et al., 2010; Benzerga and Leblond, 2014).

The Gurson (1977) model and its extensions as well as other damage-based models have been extensively used to predict failure for AHSS and aluminum alloys (Imbert et al., 2005; Nahshon and Xue, 2009). Earlier, Gurson model developments have focused on higher stress-triaxialities with limited application to lower stress-triaxiality states such as shear. Nahshon and Hutchinson (2008) and Xue, 2007 extended the Gurson (1977) model to incorporate the third stress invariant by introducing an extra damage term through the effect of the Lode parameter that allows for failure prediction even at zero hydrostatic tension. However, the shear-modified Gurson model is a heuristic approach that effectively converts the Gurson model into a phenomenological failure model for which the effective void volume fraction is a calibration parameter that represents the lost capacity in a unit cell under shear. Indeed, modeling the evolution of porosity at low stress-triaxiality is rather challenging given that characterization of void nucleation under shear deformation has not received much attention to-date. Alternatively, a modified Mohr Coulomb (MMC) model, proposed by Bai and Weirzbicki (2008), covers low stress triaxialities using the butterfly test. However, Benzerga et al., 2012 demonstrated that an infinite number of fracture loci exist in terms of failure strain as a function of average stress triaxiality and Lode parameter for non-proportional loadings and therefore the path-dependent phenomenological models, are therefore not capable to predict failure under non-proportional loading such as sheared edge stretching.

Sheared edge stretching is a two-stage non-proportional loading case that consists of through-thickness shearing followed by in-plane stretching. The critical step to model this complex loading condition is to capture the deformation within the shear-affected zone (SAZ) caused by the shearing operation. One strategy to account for the properties of the sheared edge is to perform a sequential simulation of the blanking operation followed by the hole expansion test, as in Hubert et al. (2012) who mapped predictions of plastic strain resulting from the shearing process to the edge stretching simulation. A two-step pre-damage mapping model was proposed by Wang et al. (2015) to transfer the equivalent strain obtained from shearing simulations to hole expansion simulations, however, such approaches are computationally expensive and the strain distribution predicted by shearing simulations should be validated. Recently, Kahziz et al. (2016) characterized the damage evolution behind the DP600 sheared edge and suggested the need for a sophisticated model that can reproduce the mechanics of the sheared edge by taking into account damage nucleation for different stress-states and work-hardening introduced during the shearing process.

The objective of the current work is to develop a micromechanics-based fracture model to predict cracking during hole tension testing of sheared holes within CP800 and DP780. The approach differs from previous research in that measured shear strain distributions taken from the SAZ of these alloys (Pathak et al., 2019) are used to initialize the finite element model of the hole thus avoiding the requirement to simulate the actual shearing process. Analytical models are applied to integrate the damage development corresponding to the local shear strains which is also used to initialize the hole tension simulation. The subsequent damage development and fracture of the hole tension samples is simulated and compared to predictions for drilled and reamed holes for which there is no SAZ. The damage and ductility predictions are compared to tomography measurements on the sheared hole tension samples interrupted at various strain levels prior to fracture. These results are compared to previous measurements on reamed hole tension samples reported by Pathak et al. (2019b) in order to isolate the role of damage stemming from the shearing process on edge formability.

2. Experiment methodologies

2.1. Material characterization

The relevant mechanical properties along the rolling (RD), transverse (TD) and diagonal (DD) directions are listed in Table 1 and have been characterized in previous work (Pathak et al., 2016).

Table 1
Mechanical properties of the CP800 and DP780 steels. The standard deviation after three tests is indicated in the bracket (Pathak et al., 2016).

Material	Thickness (mm)	Direction	Yield strength (MPa)	Ultimate Tensile Strength (MPa)	Total Elongation (%)	n	Reduction of Area (%)
CP800	2.90	RD	710 (6)	810 (3)	19.6 (1.7)	0.08 (0.00)	69 (6)
		TD	788 (5)	850 (5)	18.8 (1.0)	0.06 (0.00)	
		DD	726 (8)	800 (5)	20.5 (2.0)	0.07 (0.00)	
DP780	1.56	RD	509 (8)	800 (6)	22.8 (2.2)	0.16 (0.00)	41 (4)
		TD	522 (4)	806 (5)	21.6 (1.8)	0.15 (0.00)	
		DD	533 (6)	815 (8)	25.5 (1.8)	0.15 (0.00)	

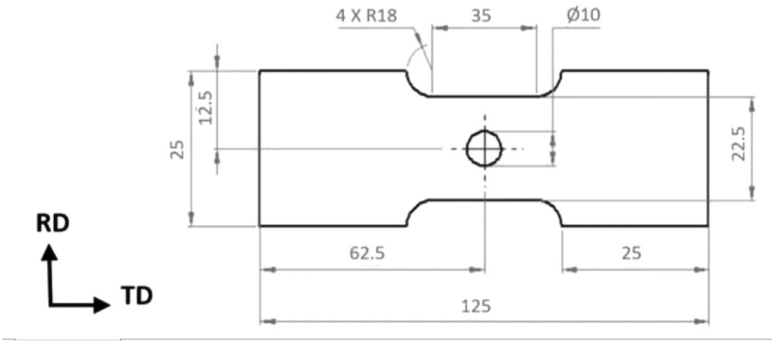

Fig. 1. A specimen geometry of the DP780 hole tension test. All units are in mm.

2.2. Hole tension test

Hole tension specimens (Fig. 1) were adopted to characterize failure strain under uniaxial loading (Bai and Wierzbicki, 2008; Anderson et al., 2017;) as well as to characterize edge-stretchability (Wang et al., 2015; Pathak et al., 2019). Unlike the hole expansion test where the hole is deformed out-of-plane, hole tension specimens experience in-plane deformation which eases specimen preparation for the tomography-based damage measurements. The geometry of the hole tensile test has a reduced section length of 35 mm with a 10 mm diameter hole at the center as shown in Fig. 1. The width of the ligament on either side of the hole was selected as four times the material thickness for the two materials investigated.

Two sets of specimens were studied for both the materials using two different hole processing techniques: reamed and sheared. The holes were processed using the techniques adapted in previous work (Pathak et al., 2017). The hardness measurement conducted behind the reamed edge indicates that minimal work-hardening exists behind the reamed edge and therefore formability of reamed edge is directly related to the microstructure of the material. In contrast with the reamed edge, the hardness values behind the sheared edge (Fig. 2) peak at the edge and then decreases to the value of base material and, suggests the presence of work-hardening introduced during the shearing process.

The specimen was subjected to tension in a 100 kN MTS Criterion model 45 servo-electric tensile frame at a cross-head displacement of 0.075 mm/s. *In situ* 3-D digital image correlation (DIC) measurements (Correlated Solutions Inc.) were used to record the full-field strain distribution using a frame rate of 4 images per second and image size of 2448 × 2048 pixels. A vertical virtual extensometer of length 18 mm was used to define a nominal strain measure. This gauge length and cross-head velocity correspond to a nominal strain rate of 0.003 s^{-1}. The DIC images were analyzed using a resolution of 0.02 mm/pixel, with a filter size and step size of 9 and 3 pixels, respectively. These correspond to a Virtual Strain Gauge Length (VSGL) of 0.50 mm:

$$\text{VSGL} = \text{Step size} \times \text{Filter size Resolution of the area of interest} \times \tag{1}$$

The equivalent strain history was calculated based on von Mises plasticity theory and plastic volume conservation by integrating

$$d\varepsilon = \frac{2}{\sqrt{3}}\sqrt{\left(d\varepsilon_1^2 + d\varepsilon_2^2 + d\varepsilon_1^2 d\varepsilon_2^2\right)}, \tag{2}$$

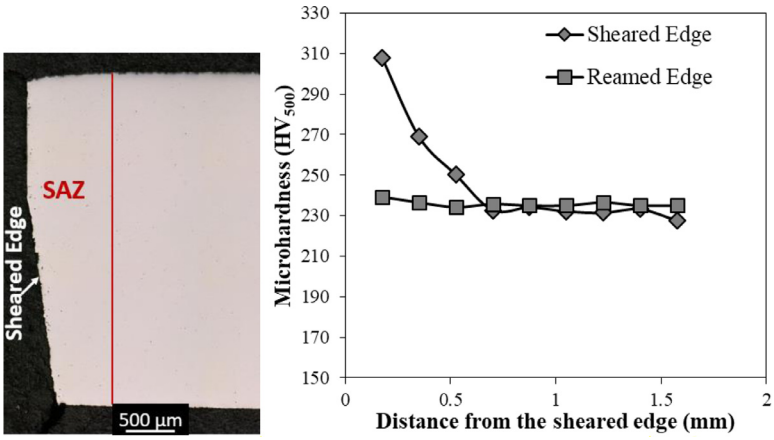

Fig. 2. The hardness profile for the DP780 reamed and sheared edges in the rolling direction.

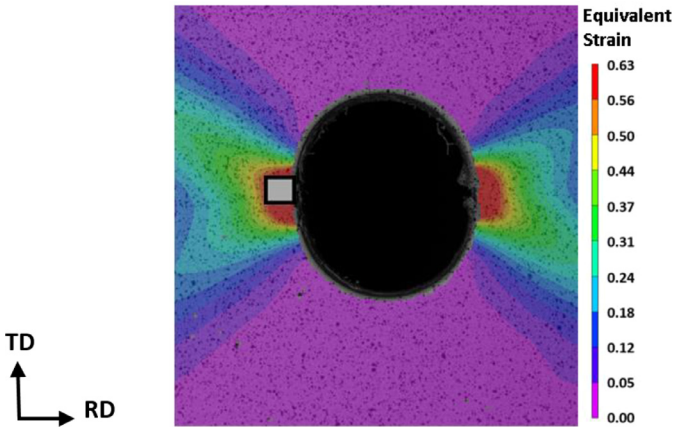

Fig. 3. Measured contours of equivalent strain during the CP800 sheared hole tension test just prior to fracture a nominal strain rate of 0.003s-1.

to determine the total equivalent strain, ε_{eq}, directly from the DIC measurements. A typical contour plot of measured equivalent strain for a DP780 reamed hole tensile specimen is shown in Fig. 3. The maximum deformation occurs along the hole edge at center and the failure is reported to be initiated from the area indicated by grey square.

2.3. Tomography

The tomography specimens of cross-section 500 µm X500 µm and length 700 µm were extracted from the maximum deformed region of each interrupted specimen, as indicated by the grey colored square in Fig. 3. The samples were ground to a thickness of approximately 0.7 mm followed by cutting to the desired cross-section, using an Accutom precision cutter and a continuous water supply to avoid heating of the sample. A EasyTom system at the MATEIS laboratory in INSA Lyon was used to acquire tomographs of the specimens. The tomograph was operated at 100 kV and 75 μA to obtain voxel size of 1 µm. The noise associated to the scan acquisition was reduced by applying median filter with a radius of two voxels to the reconstructed volumes. The volumes were thresholded to differentiate the void phase from the steel phase. The edge surface was detected using an ImageJ plugin (Abràmoff et al., 2004) that highlights sharp changes in intensity in 3D binarized volumes. The 3D visualization was done using the ImageJ 3D volume viewer. Voids appear in red and the bulk material in white in the following 3D views of the reconstructed slices. To be registered as a void, a set of pixels need to be statistically significant in three dimensions; therefore, voids with the diameter less than twice the voxel size i.e. 2.0 µm were excluded from the analysis. The void quantification was conducted using ImageJ to provide measurements of the morphology of each individual void within a specimen. Due to the high cost involved in conducting tomography scans, no repeats were performed and hence considered as a limitation of the current work.

Table 2
Equivalent failure strain and displacement to failure for the sheared holes.

Materials	Equivalent Strain				
	1	2	3	4	Fracture
CP800	0.26	0.48	0.52	0.55	0.61± 0.04
DP780	0.16	0.18	0.20	0.22	0.28± 0.04

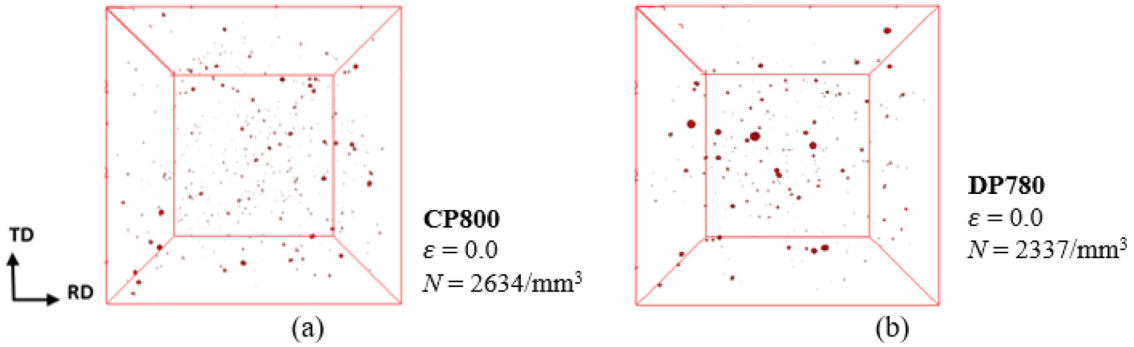

Fig. 4. 3D views of damage within as-sheared edges of the CP800 and DP780 steels.

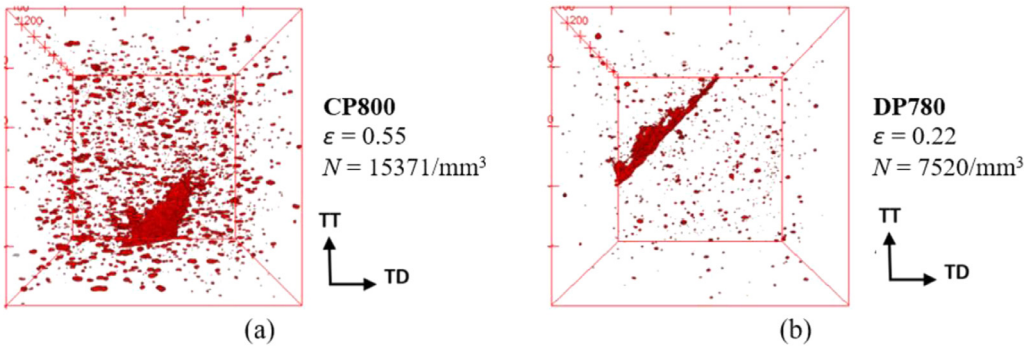

Fig. 5. 3D views of damage within the CP800 and DP780 sheared hole tension specimens near failure.

3. Damage evolution during the edge stretching

To systematically characterize the damage mechanisms during sheared edge hole tensile testing, interrupted testing was conducted at four different nominal strain levels for the sheared CP800 and DP780 samples. The local equivalent strain from the DIC measurements for each interrupted specimen are indicated in Table 2. Tomography specimens were extracted from each interrupted specimen at the location shown in Fig. 3.

Figs. 4 and 5 shows the tomograms of the CP800 and DP780 taken from the as-sheared specimens ($\varepsilon = 0$) and hole tension specimen interrupted closest to failure, respectively (tomograms from the specimens interrupted at intermediate deformation levels are not shown for brevity). The number of voids nucleated per mm^3 (N) and von Mises equivalent strain (ε) are indicated. The tomograms near failure show extensive void damage and early stages of cracking through void coalescence for both materials. Note that the strain level in the DP780 sample near failure (Fig. 5(b)) is less than one-half of the strain in the CP800 sample (Fig. 5(a)), reflecting a higher damage level in the DP780. 3D views are defined using RD, TD and TT (through-thickness) axes.

To provide baseline data against which the sheared edge damage rates could be assessed, damage rates from tomograms extracted from drilled and reamed specimens reported by Pathak et al. (2019b) are also considered. Data from these samples are labelled as “reamed” whereas the current samples are referred to as “sheared” in the following discussion.

3.1. Void nucleation histories

Fig. 6 shows the effect of edge condition on the progression of void nucleation, expressed here in terms of the number of voids per unit volume as a function of equivalent strain for both materials. The number of voids at a particular strain

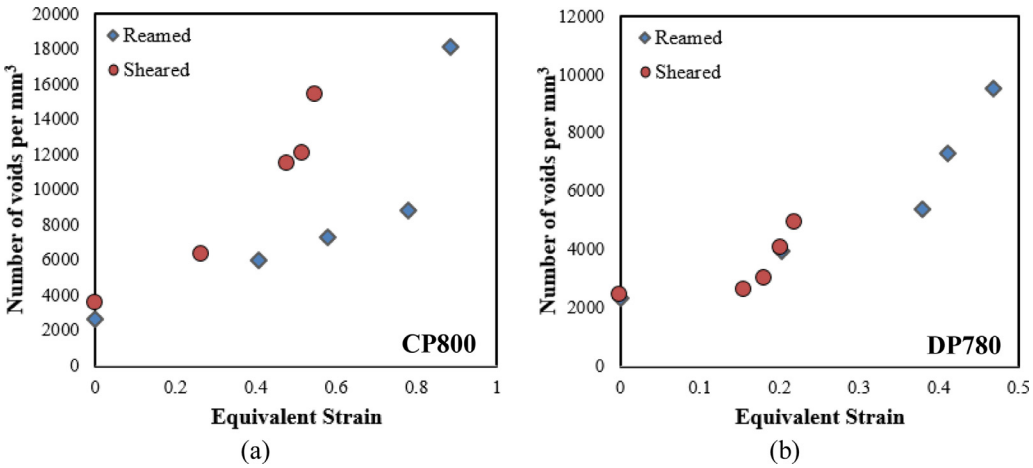

Fig. 6. Average void density versus equivalent strain for (a) CP800 and (b) DP780 sheared versus reamed edges. Void density data from the reamed samples is from Pathak et al. (2019b).

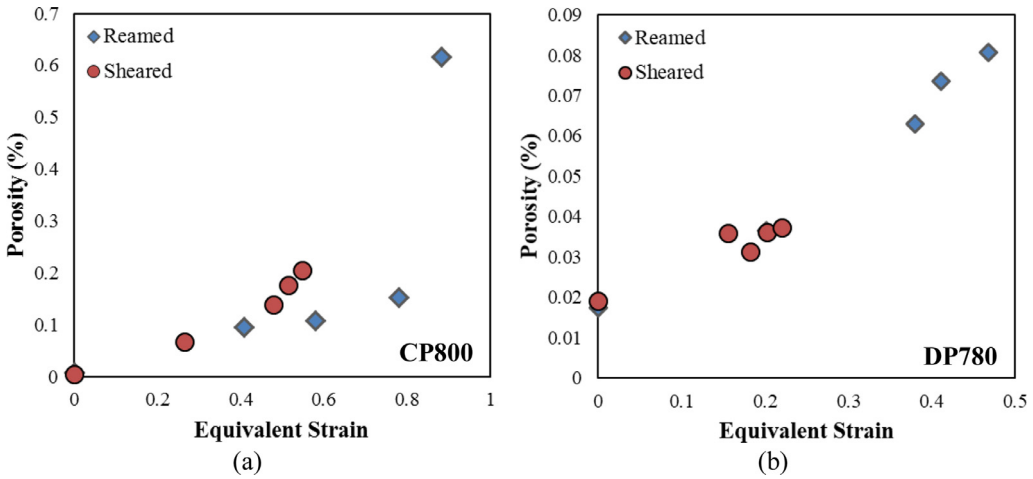

Fig. 7. Evolution of the porosity with respect to equivalent strain for (a) CP800 and (b) DP780. Reamed edge data is due to Pathak et al. (2019b).

is considerably higher behind the sheared edge compared to the reamed edge. The work-hardening generated during the shearing process within the SAZ leads to an increase in the subsequent rate of nucleation at the sheared edge compared to the reamed edge for the CP800 and DP780 steels.

3.2. Porosity histories

Porosity is defined as a total void volume divided by the total volume considered and is presented as a function of the equivalent strain for both materials in Fig. 7. With an increase in strain, damage accumulation increases due to the continuous nucleation of voids and their subsequent growth and coalescence. The porosity is higher behind the sheared edge compared to the reamed edge due to the higher nucleation rate. A higher rate of damage evolution within the ferritic-martensitic DP780 microstructure is reported due to a higher strength-differential within the ferritic matrix resulting in rapid void nucleation compared to the CP steels that has a less strength differences between bainite and ferrite phases. Similar trends were reported based on 2D damage quantification using optical metallographic techniques applied to the same alloys (Pathak et al., 2017).

3.3. Void growth

Fig. 8 shows the average equivalent diameter of voids at the sheared versus reamed edges as a function of equivalent strain for the reamed and sheared edges. The increase in void diameter with strain is similar for the shear and reamed CP800 samples. The DP780 exhibits very little change in void diameter during the deformation of both the edges. A similar observation was reported by Avramovic-Cingara et al. (2009) and Landron et al. (2013) for a DP600 steel. This trend is

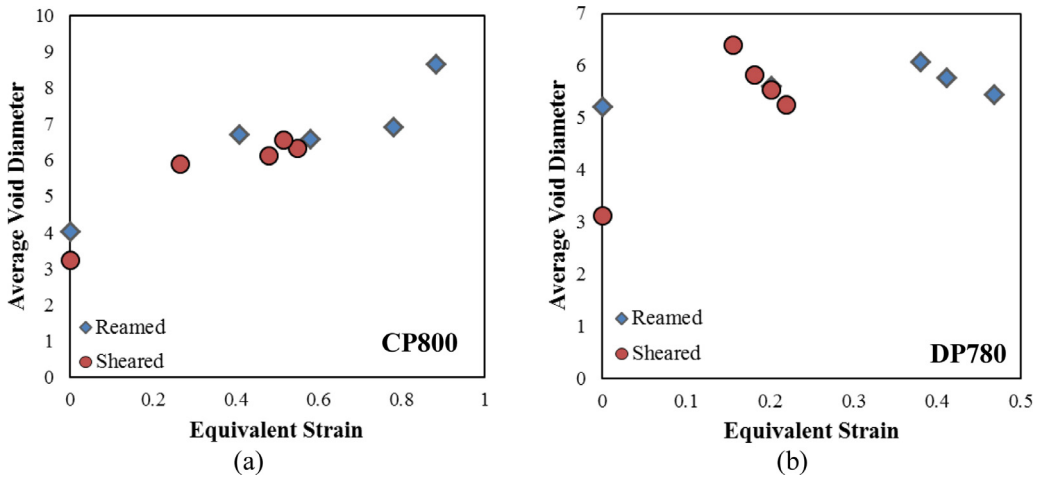

Fig. 8. Average void diameter versus equivalent strain for (a) CP800 and (b) DP780 reamed and sheared edges.

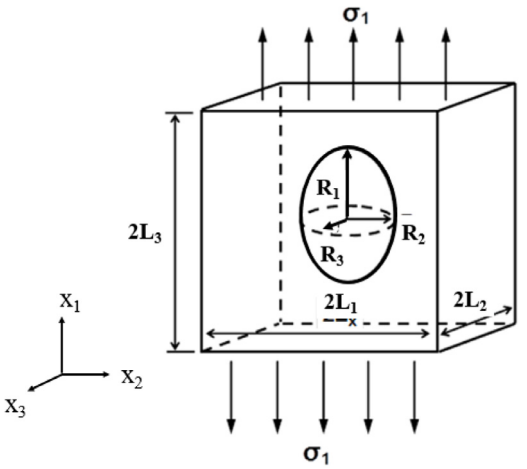

Fig. 9. An illustration of ellipsoidal void.

accounted to the continuous nucleation of smaller voids throughout the deformation, the newer smaller voids balancing the increase in average diameter induced by growth of existing voids.

For further analysis of the void growth, individual voids were approximated as being ellipsoidal in shape with semi-major axes R_1, R_2 and R_3, as illustrated in Fig. 9. The largest semi-major axis, R_1, is aligned with the loading direction along coordinate axis x_1.

The void aspect ratio is defined as R_1/R_2. The voids were approximated as ellipsoidal and the void diameter along the x_2 and x_3 axes are averaged for the reamed condition. Therefore, the void aspect ratio can be defined as R_1/R_{avg} where R_{avg} is the average radius of R_2 and R_3. A slight increase in void aspect ratio was observed for the CP800 steel near the failure strain while it remained almost constant for the DP780 steel as shown in Fig. 10.

3.4. Void spacing evolution

Models of void coalescence, such as the model proposed by Thomason (1999), demonstrate that the necking failure of the inter-void ligament between neighboring voids is strongly dependent on the void aspect ratio and the relative void spacing. Fig. 11 presents the void spacing, defined here as the center-to-center distance between the nearest neighboring voids, with respect to strain for the CP800 and DP780 reamed and sheared holes. A decrease in void spacing was observed with an increase in strain for the two edge conditions and materials. This occurs naturally due to the lateral contraction of the sample during tensile straining. In addition, the number of nucleated cavities increases with deformation and subsequent occurrence of voids at a shorter distance and consequently decreases void spacing. Interestingly, the initial void spacing is smaller for the sheared edge compared to the reamed edge due to the nucleation of voids nucleated during the shearing process.

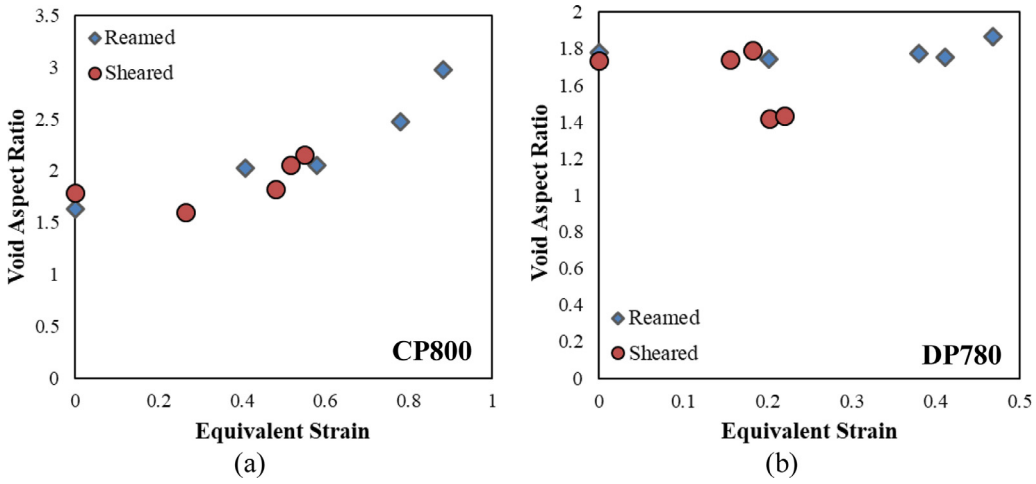

Fig. 10. Variation of the void aspect ratio with equivalent strain for (a) CP800 and (b) DP780.

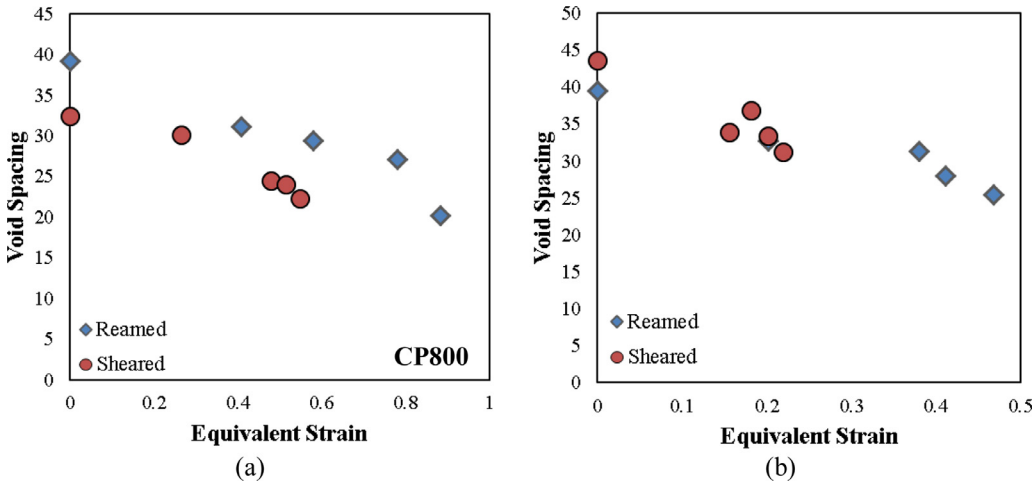

Fig. 11. Variation of the average center-to-center void spacing with the equivalent strain for (a) CP800 and (b) DP780.

4. Material modeling

The experimental results presented in the previous sections indicate that damage development through nucleation, growth and coalescence of voids, at the sheared or reamed edges is continuous in the two steels. To predict damage accurately, an analytical model for each stage of the void evolution is adapted and discussed below. The results presented in the previous section suggest that the void volume fraction is quite low (<0.3%) until the onset of coalescence and that void-induced softening is minor. In addition, the triaxiality at a free edge will be one of uniaxial tension until late in the deformation process when necking can occur. These two factors favor the adoption of an uncoupled micromechanics-based fracture model, as presented in this section.

4.1. Constitutive response

The degree of anisotropy displayed by the two alloys is relatively mild as seen in the constitutive characterization results of Pathak et al. (2019b). Their data is summarized in Table 2 and includes *r*-values along the three characteristic material directions (RD, TD, DD), as well as the ratios of yield strength along the TD and DD directions normalized by the RD yield strength.

In general, the *r*-values and stress ratios are all relatively close to unity, suggesting that complex yield functions are not needed to model this material. As a result, the moderate anisotropy of the CP800 and DP780 steels was modeled using Barlat Yld91 yield function (Barlat et al., 1991), expressed as:

$$\sigma = \left(0.5\left(|S_1 - S_2|^m + |S_2 - S_3|^m + |S_3 - S_1|^m\right)\right)^{1/m} \tag{3}$$

Table 3
Stress-ratios and r-values from tensile tests along the rolling, diagonal and transverse directions (Pathak et al., 2019b).

Material	σ_{DD}/σ_{RD}	σ_{TD}/σ_{RD}	τ/σ_{RD}	r_{RD}	r_{DD}	r_{TD}
CP800	0.98	1.08	0.63	0.70	0.95	1.33
DP780	1.00	1.00	0.50	0.72	0.92	0.98

Table 4
The parameters of Yld91 yield function for the CP800 and DP780 steels (Pathak et al., 2019b).

Material	*a*	*b*	*c*	*h*	*g*	*f*
CP800	−0.81	0.85	0.12	1.00	1.00	−1.04
DP780	−1.00	0.60	0.47	1.00	1.00	0.99

Table 5
Swift's hardening law parameters for the CP800 and DP780 steels.

Material	K	ε_o	n	R^2
CP800	1022	0.0057	0.07	0.99
DP780	1261	0.004	0.16	0.96

where $m = 6$ is chosen based on the body centered cubic crystallographic structure. S_1, S_2 and S_3 are eigenvalues of deviatoric stress tensor **S**. The yield function parameters of Yld91 (*a, b, c, h, g* and *f)* were also determined by Pathak et al. (2019b) based on the data in Table 3. The values of the parameters are given in Table 4

The hardening response for this material was also fit to a Swift hardening law by Pathak et al. (2019),

$$\sigma = K(\varepsilon o + \varepsilon^p)^n \tag{4}$$

where ε_o is the initial strain, ε^p is the Von mises equivalent plastic strain, σ_y is the initial yield stress, K and n are the material parameters that describes the rate of hardening. Table 5 indicates the Swift hardening parameters adopted in this work. The R^2 value of 0.96 and 0.99 indicates strong correlation of the fitted hardening law and experimental data up to UTS.

For constitutive modeling, the material derivatives of stress and strain $(\acute{\varepsilon}, \acute{\sigma})$ have to be independent of rigid body rotation and therefore the objective co-rotational rate of a stress or strain tensor, ε° and σ°, are used as expressed by

$$\varepsilon^\circ = \acute{\varepsilon} + \varepsilon\Omega - \Omega\varepsilon \tag{5}$$

$$\sigma^\circ = \acute{\sigma} + \sigma\Omega - \Omega\sigma \tag{6}$$

where Ω is the spin tensor. A numerical integration of the constitutive model to large strain levels is performed using the logarithmic spin tensor proposed by Xiao et al. (1997). The objective update of stress and strain tensors at time t_{n+1} are performed using the mid-point integration algorithm proposed by de Souza Neto et al. (2011), expressed as:

$$\sigma_{n+1} = \Lambda_\alpha \sigma_n \Lambda_\alpha^T + L : \Lambda_\beta D_{n+1/2} \Lambda_\beta^T \tag{7}$$

$$\varepsilon_{n+1} = \Lambda_\alpha \varepsilon_n \Lambda_\alpha^T + \Lambda_\beta D_{n+1/2} \Lambda_\beta^T \tag{8}$$

where $\Lambda_\alpha = \exp(\Omega^{log}_{n+1/2})$, $\Lambda_\beta = \exp(\frac{1}{2}\Omega^{log}_{n+1/2})$, D is rate of deformation and L is the fourth order tangent moduli tensor. The stress and strain tensors are updated using the objective rate and passed within the UMAT implementation using a backward Euler stress integration algorithm.

4.2. Fracture model

In this section, the adopted fracture model which includes treatment of void nucleation, growth and coalescence criteria.

4.2.1. Nucleation model

Void nucleation was modelled using an enhanced version of Chu and Needleman's (1980) model that was introduced by Pathak et al. (2019b) to account for stress-triaxiality and Lode parameter as:

$$\acute{N} = \frac{N_n}{s_N\sqrt{2\pi}} exp\left[\frac{-1}{2}\left(\frac{\varepsilon_p - \varepsilon_N(T,L)}{s_N}\right)^2\right]\varepsilon_p \tag{9a}$$

Table 6
Material parameters for the CP800 and DP780 steels listed in Eq. (10).

Material	C_1	C_2	C_3	C_4	C_5
CP800	0.44	1.7	0.7	2.2	1.8
DP780	1.80	901.5	0.7	1409.0	1.7

$$s_N = c_v \varepsilon_N \tag{9b}$$

where $\acute{N}$ is the void nucleation rate per unit volume, N_n is the maximum number of voids per unit volume available to nucleation voids, ε_N, s_N and c_v are the mean, standard deviation and coefficient of variance of the nucleation strain. ε_N is the mean nucleation strain which Pathak et al. (2019b) expressed as a function of stress-triaxiality and Lode parameter utilizing the function form of Luo and Wierzbicki (2010) fracture locus, expressed as:

$$\varepsilon_N = \left\{ \begin{array}{l} \frac{C_1}{C_2}\left[C_3 + \frac{\sqrt{3}}{2-\sqrt{3}}(1-C_3)\left(\sec\left(\frac{\pi L}{6}\right)-1\right)\right] \\ \times\left[\sqrt{\frac{1+C_4^2}{3}}\cos\left(\frac{\pi L}{6}\right) + C_4\left(T + \frac{1}{3}\sin\left(\frac{\pi L}{6}\right)\right)\right] \end{array} \right\}^{\frac{-1}{C_5}} \tag{10}$$

where C_{1-5} are the material parameters developed by Pathak et al. (2019b) for these alloys are listed in Table 6.

4.2.2. Growth model

Ragab (2004) developed a model of void growth based upon a modification to the q_i-coefficients introduced by Tvergaard (1981) within the well-known (Gurson, 1975, 1977) yield function. The growth rate of the voids is proportional to the maximum principal strain rate expressed as

$$\acute{f}_{growth} = \frac{3f(1-f)q_1q_2\sinh\left(q_2\frac{3}{2}\frac{\sum_{hyd}}{\acute{\sigma}}\right)}{3\left(\frac{\sum_1 - \sum_{hyd}}{\acute{\sigma}}\right) + fq_1q_2\sinh\left(q_2\frac{3}{2}\frac{\sum_{hyd}}{\acute{\sigma}}\right)}\acute{\varepsilon}_1 \tag{11}$$

The semi-empirical equations of Ragab (2004) describe the q_i-coefficients as functions of the stress-triaxiality, T, void aspect ratio, W, and hardening exponent, n:

$$q_1 = A + BT + CT^2 + DT^3 \tag{12}$$

$$A = 2.28 - 3.35n + 3.84n^2 \tag{13}$$

$$B = -0.92 + 1.32n - 0.32n^2 \tag{14}$$

$$C = 0.53 - 2.31n + 2.35n^2 \tag{15}$$

$$D = -0.10 + 0.27n + 0.70n^2 - 1.78n^3 \tag{16}$$

$$q_2 = W^{\eta} \tag{17}$$

$$\eta(W < 1) = 0.206\ln(T) - 0.266 - 0.02n \tag{18}$$

$$\eta(W \geq 1) = -3.484 + 11.614T - 13.72T^2 + 6.54T^3 - 1.06T^4 + 0.2n \tag{19}$$

As shown previously in Fig. 10, the void aspect ratio remains almost constant until close to the failure for both sheared and reamed edge conditions. Therefore, in the numerical model, the void shape was assumed to be ellipsoidal and remain constant during deformation with a value of 1.4 and 1.8 for the DP780 and CP800 steel, respectively.

4.2.3. Coalescence model

The plastic limit-load (PLL) approach of Thomason (1990) was adopted to predict the onset of void coalescence mechanism due to necking failure of the inter-void ligament, transverse to the principal loading direction. Several extensions of Thomason's PLL model have been proposed (Pardoen and Hutchinson, 2000; Zhang et al., 2005; Benzerga, 2002; Benzerga and Leblond, 2014) and have reported to provide excellent agreement for unit cell simulations. Recently, Benzerga and Leblond (2014), have obtained the first closed-form analytical solution for void coalescence by internal necking where coalescence occurs when

$$\frac{\sigma_b}{\sigma_y} \geq C_f(\chi, W) = \frac{1}{\sqrt{3}}\left[2 - \sqrt{1+3\chi^4} + ln\left[\frac{1+3\chi^4}{3\chi^2}\right]\right] + \frac{1}{3\sqrt{3}}\left[\frac{\chi^3 - 3\chi + 2}{\chi W}\right] \tag{20}$$

where σ_b is the maximum principal stress, σ_y is the yield stress, W is the void aspect ratio, and χ is the ligament size ratio defined as the ratio of the lateral void radius, R_i, to the lateral void spacing, L_i, for a 3-D unit cell as shown in Fig. 9.

The geometrical relationship of the unit cell to describe the microstructure of a voided unit cell and the porosity in the unit cell is given in Butcher (2011) and expressed as

$$\frac{f}{\gamma} = \frac{V_{void}}{V_{cell}} = \frac{R_1R_2R_3}{L_1L_2L_3} = \chi_1\chi_2\chi_3 = \frac{W_1W_2}{\lambda_1\lambda_2}\chi_2^3 \tag{21}$$

where W_i are the void aspect ratios; λ_i are the cell aspect ratios; χ_i are the void spacing (or ligament size) ratios and γ is a shape parameter specific to the assumed unit cell with $\gamma = 2/3$ for an axisymmetric unit cell and $\gamma = \pi/6$ for a cubic cell (Butcher, 2011).

Taking the derivative of Eq. (21)

$$\frac{\dot{f}}{f} = \frac{\dot{R}_1}{R_1} + \frac{\dot{R}_2}{R_2} + \frac{\dot{R}_3}{R_3} - \dot{\varepsilon}_1 - \dot{\varepsilon}_2 - \dot{\varepsilon}_3 \tag{22}$$

From volume conservation Eq. (22) can be expressed as:

$$\frac{\dot{f}}{f} = \frac{\dot{R}_1}{R_1} + \frac{\dot{R}_2}{R_2} + \frac{\dot{R}_3}{R_3} \tag{23}$$

Since the void shape remains almost constant during deformation as shown in Fig. 10, the void shape is assumed to remain constant which leads to

$$\frac{\dot{R}_1}{R_1} = \frac{\dot{R}_2}{R_2} = \frac{\dot{R}_3}{R_3} \tag{24}$$

The derivative of void spacing ratio can be expressed as:

$$\frac{\dot{\chi}_i}{\chi_i} = \frac{\dot{R}_i}{R_i} - \dot{\varepsilon}_i \tag{25}$$

Using Eqs. (22)–(24), the expression for the void spacing evolution simplifies to:

$$\frac{\dot{\chi}_i}{\chi_i} = \frac{1}{3}\frac{\dot{f}}{f} - \dot{\varepsilon}_i \tag{26}$$

The plastic limit load criteria in Eq. (20) was derived for an axisymmetric unit cell so an equivalent void spacing ratio transverse to the principal loading direction can be defined as

$$\chi_{eq} = \frac{R_{eq}}{L_{eq}} = \frac{\sqrt{R_2R_3}}{\sqrt{L_2L_3}} = \sqrt{\frac{R_2R_3}{L_2L_3}} = \sqrt{\chi_2\chi_3} \tag{27}$$

This formulation for the void spacing evolution naturally lends itself towards experimental validation since void spacing ratios can be quantified from the tomography data. The void spacing ratios for both materials and edge conditions were characterized experimentally using the following procedure: First the void spacing along the directions transverse to the loading direction, L_i, are computed and the measured void spacings are presented in Fig. 11. In addition, (Benzerga, 2002) observed that necking failure of ligament generally occurred first between larger voids. To mimic this behavior, an average radius of voids was calculated for the 20 largest cavities of the studied sub-volume (as described in Landron et al. (2011)) and was used to determine the void spacing ratio, expressed as:

$$\chi_i = \frac{R_{20_i}}{L_i} \tag{28}$$

The measured void spacing ratio of an undeformed material was defined as an initial condition in the numerical model and the predicted evolution of spacing ratios is performed using equations. This approach is validated against the measured spacing ratios for deformed samples in Section 6, below.

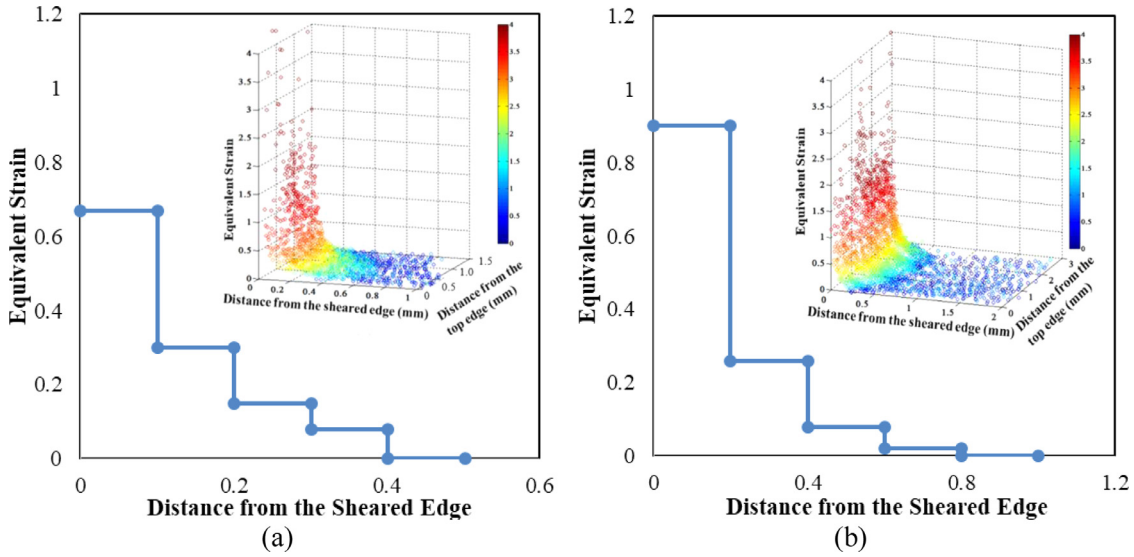

Fig. 12. Strain distribution as a function of distance from the sheared edge and top edge and thickness gradient for the (a) CP800 (b) DP780 sheared edge at 12% clearance.

4.3. Shear-affected-zone integrator

The final aspect of the damage model is to define the pre-strain introduced during the sheared edge using so-called "SAZ integrator". The measured strains from metallurgical investigation of sheared edges by Pathak et al. (2019) were used to map strains, work hardening and damage onto the elements on the shear edge. The measured strain distributions as a function of distance from the sheared edge and specimen surface (for the current 12% clearance case) are shown in the inset image of Fig. 12 for the CP800 and DP780 steels. The distributions were mapped onto sub-regions of size 0.2 mm and used to initialize the finite element model and are also plotted in Fig. 12 for the CP800 and DP780 sheared edge cases. The measured strain-distributions were mapped onto the elements at the sheared edge, as part of the UMAT subroutine with the following procedure:

1. A FORTRAN code was written to prescribe the equivalent strain to the integration points within an element, based upon the distance of the integration point from the sheared edge. The coordinates of the sheared edge face are input into the SAZ integrator to enable this calculation. The measured strain-distribution (Fig. 12) is defined in LS-DYNA using a load curve as a function of distance from the sheared edge. The depth of the SAZ is calculated using the load curve data and a check is performed for each element to determine if it lies within the SAZ or not.
2. The equivalent strain is assigned and converted into a shear angle α using the relation proposed by Butcher and Abedini (2017) and expressed as:

$$\alpha = \tan^{-1}\left\{2\sinh\left(\frac{\sqrt{3}}{2}\varepsilon_{eq}\right)\right\} \tag{29}$$

With the equivalent strain identified, a simple shear deformation is then analytically performed to the integration point using small increments of shear angle, dα. For the shear loading, the deformation gradient is defined as:

$$F = \begin{bmatrix} 1 & \gamma & 0 \\ 0 & 1 & 0 \\ 0 & 0 & 1 \end{bmatrix} \tag{30}$$

where $\gamma = \tan(\alpha)$. The **F** is computed at each increment based on shear angle and stored as history variables in LS-DYNA. For simple shear, the stress state is then integrated using the anisotropic plasticity model using a hypo-elastic-plastic formulation and the logarithmic objective rate

3. The updated stress and strain tensors are then used to integrate void nucleation and microstructure evolution for each shear increment.
4. An output fileis automatically generated at the end of the analytical shear simulation by LS-DYNA which stores the deformation gradient, equivalent strain and damage history variables for each element. This file is included in the input deck of hole tension model to initialize the plastic strain (ε_{pre}) and damage (f_{pre}, χ_{pre}, R_{pre}) introduced during the shearing process. The damage variables are determined for the second stage of deformation (f_t, χ_t, R_t) based on accumulated damage to predict failure during the sheared edge stretching operations

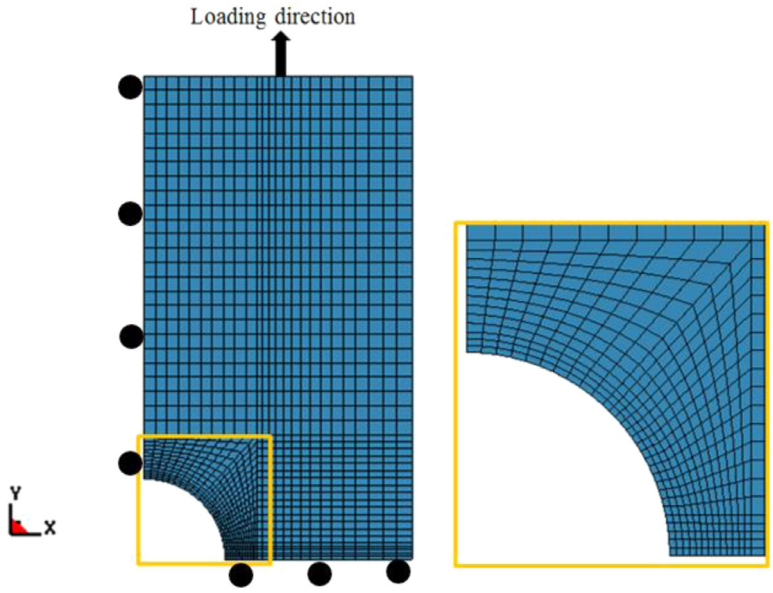

Fig. 13. Hole tension finite element mesh.

In this manner, the pre-strain and damage introduced during the shear deformation are mapped at the sheared edges of the finite element model. Since the subsequent edge stretching occurs upon an unloaded sheared edge, the residual stresses are set to zero upon completion of the SAZ integration. The equivalent plastic strain and cumulative strain tensor remain as residual strains.

5. Finite element (FE) modeling

5.1. FE model description

The micromechanics-based constitutive model was implemented into the commercial finite-element code, LS-DYNA, as a user-defined material model for explicit analysis. Due to symmetry, only one-eighth of the hole tensile geometry is represented in the finite-element model. The geometry was meshed using fully integrated solid elements with an average element size of 0.2 mm in the region near the hole edge that increased away from the hole as shown in Fig. 13. The element size near the hole edge is in agreement with the range of D values recommended by Gullerd et al. (2000) for the computational cell model. Appropriate boundary conditions were applied to account for symmetry about the XY, YZ and XZ-planes. A displacement boundary condition was enforced at the free-end of the specimen. The predicted displacement-to-failure was taken from the nodes that correspond to the half-length of the extensometer gauge length used in the DIC software. To avoid numerical issues and instabilities associated with element deletion, the elements were not deleted upon satisfaction of the coalescence criterion in Eq. (20). The simulation is terminated when coalescence mechanism occurred in all integration points.

5.2. Sheared edge initialization

Work hardening and damage in the SAZ were initialized by performing the analytical shearing operation as discussed in Section 4.2. Fig. 14 shows the distribution of strain and damage behind the CP800 and DP780 sheared edges defined as an initial condition in the hole tension model. Since the strain is the highest at the edge and decreases sharply as the distance from the sheared edge increases. The porosity is highest at the sheared edge due to void nucleation during shearing.

6. Model predictions

The load-displacement response obtained from the simulation of hole tension test is compared with the measured data in Fig. 15 and found to be in good agreement for both alloys and edge conditions. The good macroscopic agreement with both materials supports the choice of the anisotropic plasticity model (Eq. (3)). The plastic response is largely controlled by plasticity and softening is not considered. Instead, the void-based damage is used as a fracture criterion. A virtual extensometer was used to calculate the engineering strain. The nominal stress was determined by dividing the load with the minimum cross-section area. In DP780, the initiation of necking is immediately followed by crack occurrence and therefore

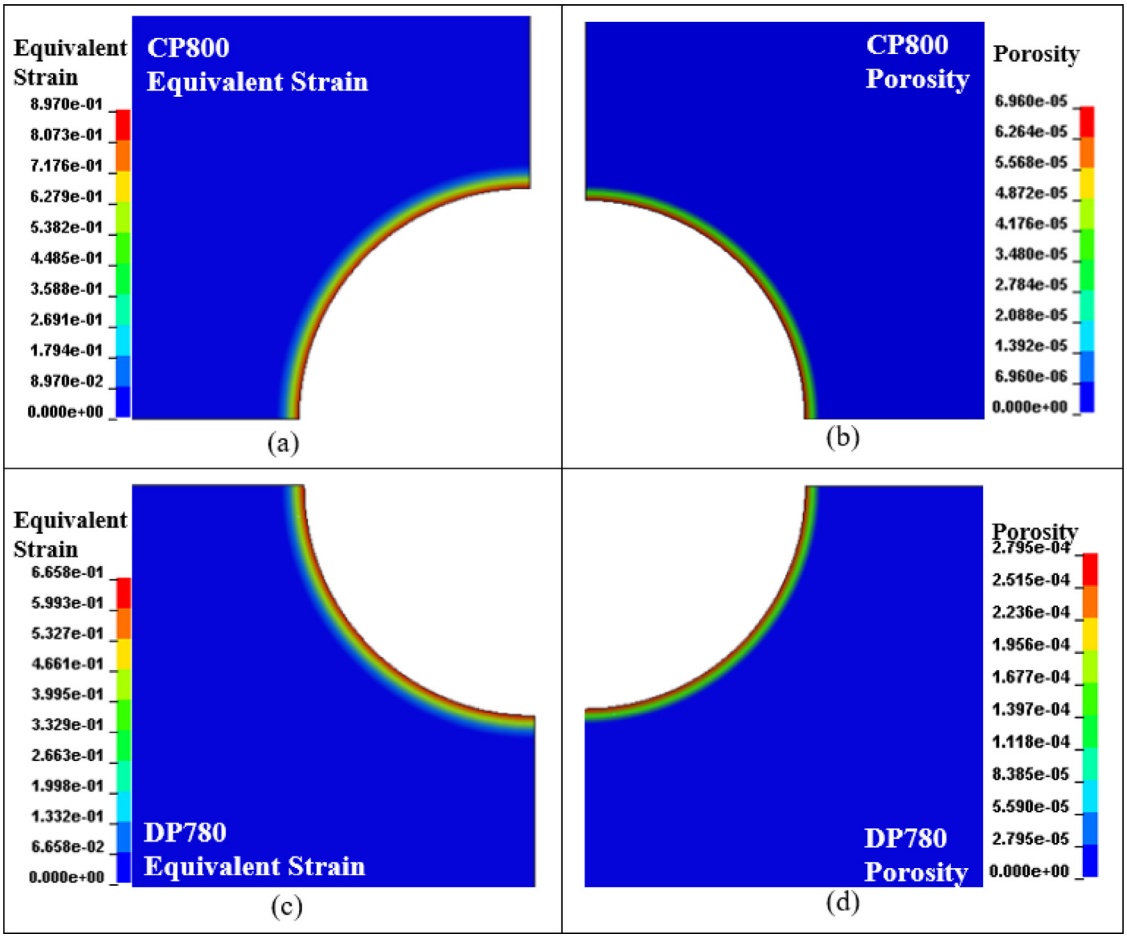

Fig. 14. Initial strain-distribution at the hole edge for (a) CP800 and (c) DP780 sheared edge and initial damage developed during shearing process behind the (b) CP800 and (d) DP780 sheared edge.

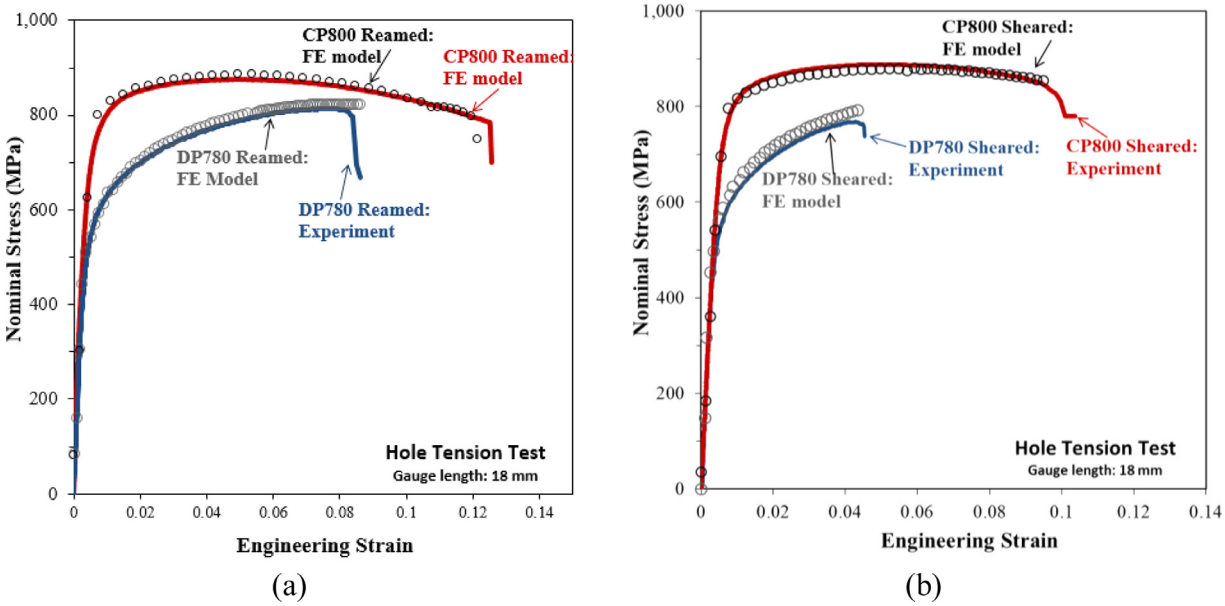

Fig. 15. Load-displacement response from the (a) CP800 and (b) DP780 hole tension tests.

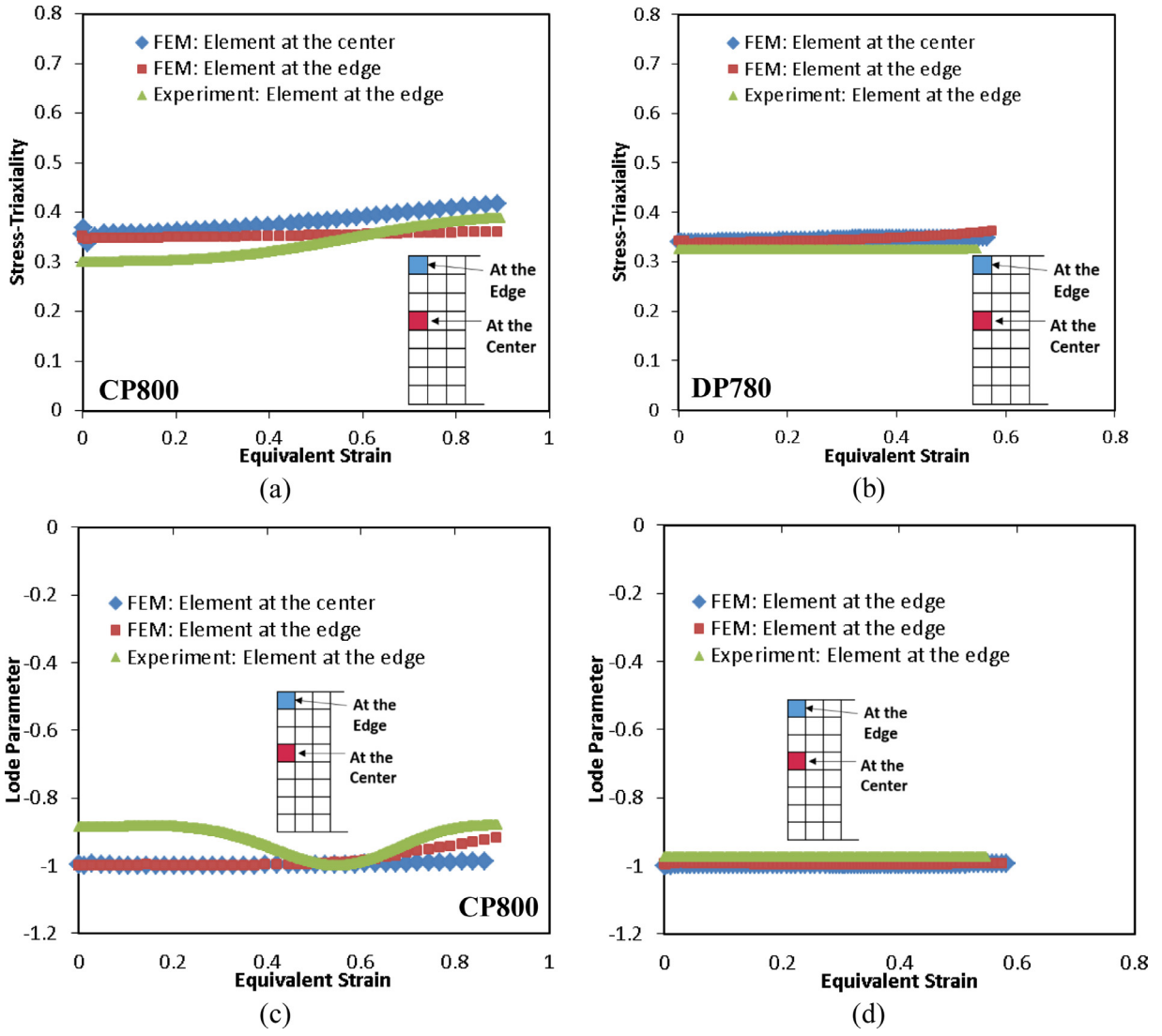

Fig. 16. Evolution of stress-triaxiality and Lode parameter as a function of equivalent strain during the reamed hole tension test for the CP800 and DP780 steels. The experimental data is reported by Pathak et al. (2019b).

the drop in load bearing capacity is very small during the deformation of the DP780 steel. The final phase of response i.e. load drop is not shown because crack propagation is not considered in the current modeling approach. The objective of this work is to measure crack initiation by predicting onset of void coalescence.

The variation of stress-triaxiality and Lode parameter during the reamed hole tension test simulation as a function of equivalent strain is shown in Fig. 16 for the element located at the center (mid-thickness) as well as located at the upper corner of the hole edge and compared with the measured data reported by Pathak et al. (2019b). The stress-state of the elements at the center (mid-thickness) as well as located at the upper corner of the expanding DP780 hole edge are approximately uniaxial tension throughout deformation with a constant stress-triaxiality of 1/3, as observed from the finite element model as well as the experimental results. The stress-state at the CP800 edge however deviates from uniaxial tension to near plane-strain and this behavior could be attributed to the higher anisotropy of the CP800 steel that causes through-thickness localization and hence the stress-state deviates from uniaxial tension. The value of Lode parameter for a uniaxial tensile stress-state is -1 and the element at mid-thickness as well as at the upper corner exhibit almost constant Lode parameter of -1 for the DP780 reamed edge which is also in agreement with the experimental result. The slight variation from uniaxial tensile stress-state was observed for the CP800 reamed edge both experimentally and numerically which could be attributed to a higher anisotropic behavior of the CP800 steel. The similar trend was followed by the corresponding sheared edge and the evolution of stress-state behind the sheared edge is not shown for brevity.

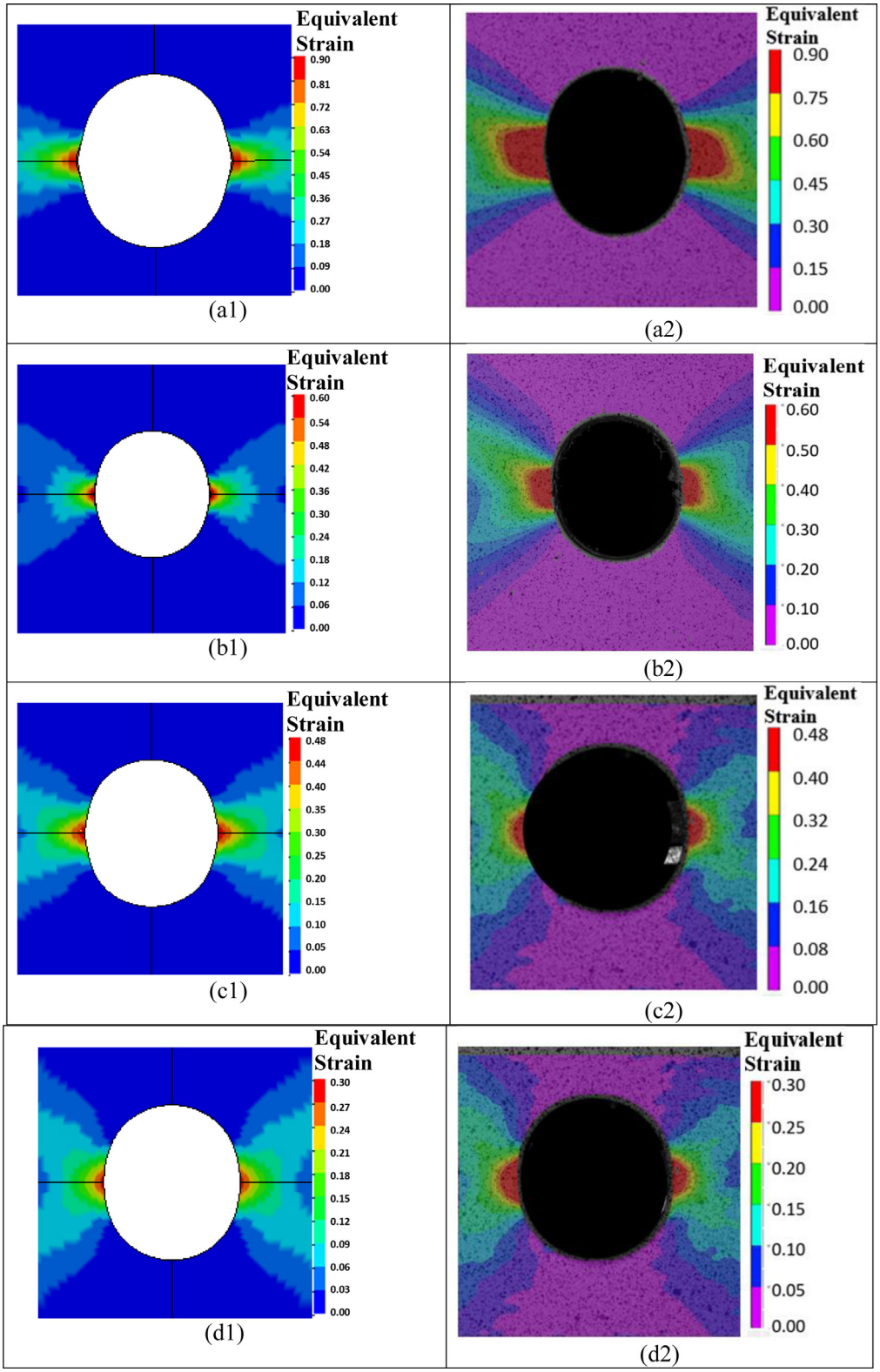

Fig. 17. Contours of equivalent strain for (a1) CP800 reamed, (b1) DP780 reamed, (c1) CP800 sheared and (d1) DP780 sheared holes just before onset of failure and the respective DIC image just before failure (a2,b2,c2 and d2).

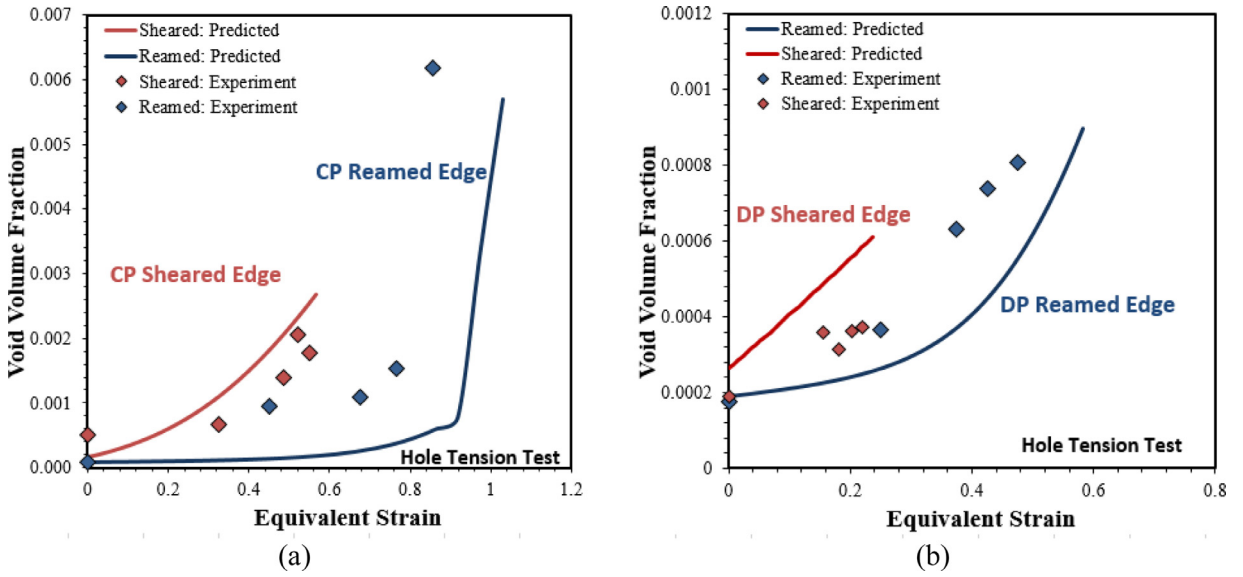

Fig. 18. Comparison of measured and predicted void volume fraction (porosity) as a function of equivalent strain for the (a) CP800 and (b) DP780 edges. Experimental data is represented by symbols and solid lines correspond to predictions.

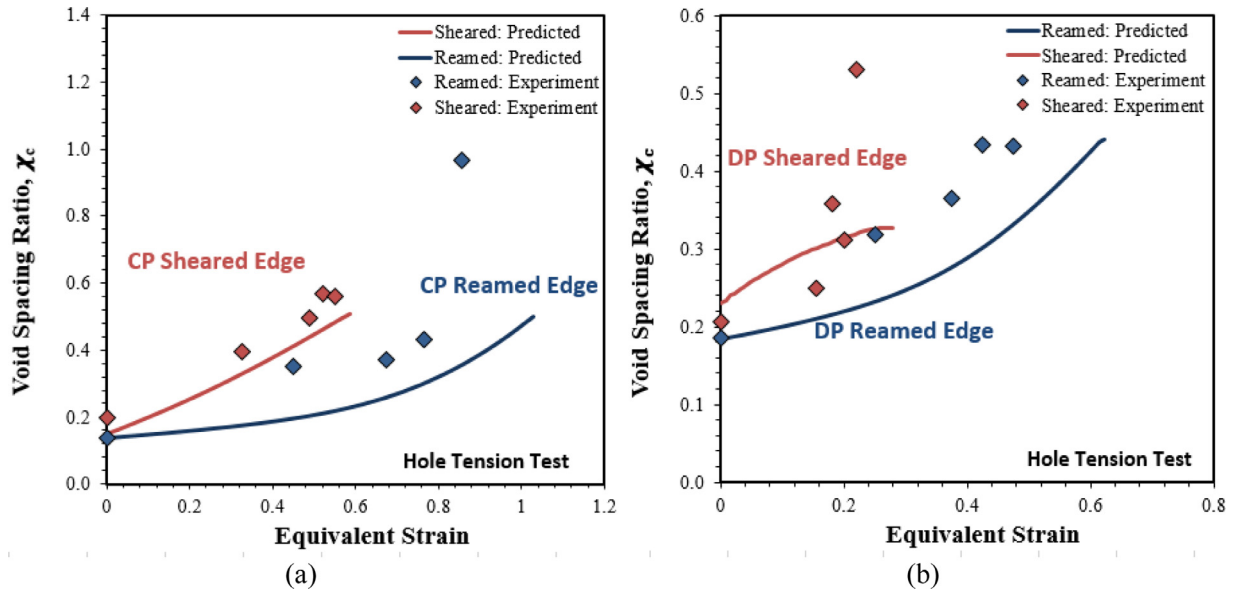

Fig. 19. Comparison of measured and predicted void spacing ratio as a function of equivalent strain for the (a) CP800 and (b) DP780 edges.

The ability of the model to capture the deformation fields for the hole tension samples can be assessed from examination of Fig. 17 which shows contours of equivalent strain from the models and experiments for both alloys and edge conditions. In general, the predicted contour plots agree reasonably well with the measured distributions.

To check the accuracy of damage accumulation predicted by the proposed damage model, the predicted evolution of porosity as a function of equivalent strain from the simulation and the measured values are shown in Fig. 18. The experimental data is represented by symbols while the solid lines are the model predictions. For consistency, the porosity is an average over several elements comprising the region where the tomography specimen was extracted. Qualitatively, the model predicts the porosity evolution reasonably well and captures the trends of accelerated damage development. The major discrepancy between the experiment and simulated data is observed for the DP780 sheared edge and could be attributed to the limited tomography resolution that fails to capture voids with a diameter smaller than 2 μm. Since the failure occurs at a low strain for the DP780 sheared edge, the void growth is very limited and hence a fraction of voids could remain undetected from the tomography scan.

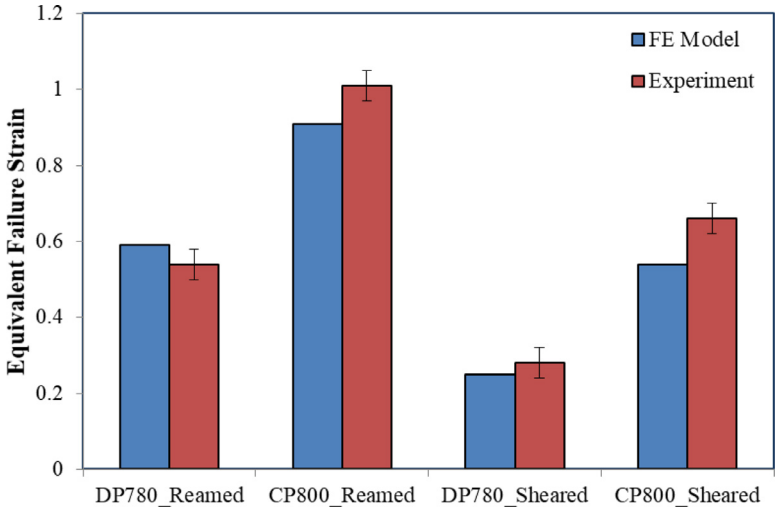

Fig. 20. The predicted and measured failure strain for the CP800 and DP780 hole tension specimens.

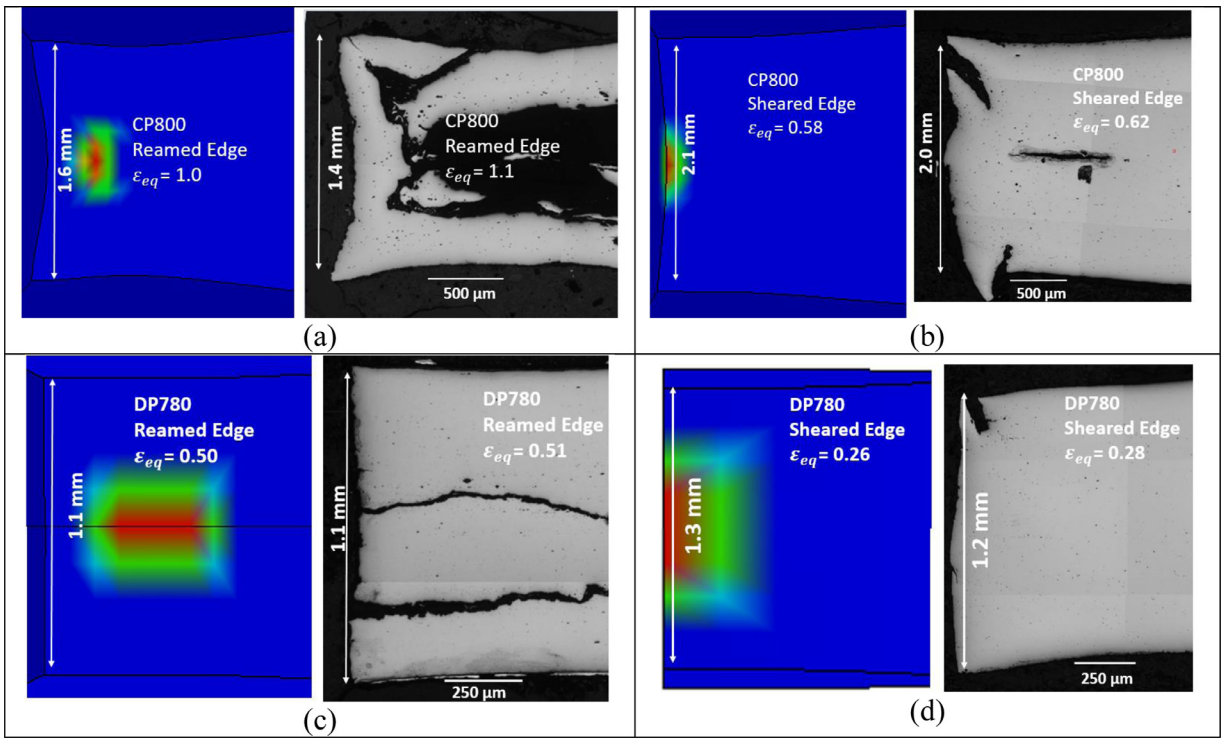

Fig. 21. Contour plots showing predicted regions of void coalescence (red contours) and corresponding specimen cross-sections: (a) CP800 reamed, (b) CP800 sheared, (c) DP780 reamed, and (d) DP780 sheared edges.

Final failure through void coalescence occurs via localization within the ligaments between neighboring voids which is dependent on the void spacing ratio. The predicted evolution of the effective void spacing ratio is compared to the measured data for the different edge conditions, as seen in Fig. 19. The predicted initial void spacing of the sheared edge is in close agreement with the measured data, indicating that the damage parameters from the proposed SAZ integrator algorithm is working well. Since the initial void spacing ratio (and void nucleation extent) differs between the reamed and sheared edges, the predicted trends also differ and are in qualitative agreement with the experimental data.

The predicted failure strains based on the void spacing ratios and the Benzera and Leblond (2014) coalescence criterion in Eq. (28) are presented in Fig. 20 along with measured failure data from the hole tension tests (Pathak et al., 2017). The predicted and measured failure strains are in close agreement, with the predicted values slightly less than the measured

values. It is important to note that the predicted failure strain is an indicator of the onset of coalescence while the measured failure strain was reported when a crack was visible, possibly accounting for the slight underestimate of failure strain. More importantly, the model captures the trends in failure strain as a function of alloy and edge condition rather well.

The finite element model of hole tension test along through-thickness direction at the initiation of failure is shown in Fig. 21. Red markers denote the onset of coalescence and failure. As demonstrated in Fig. 21, failure was predicted to initiate behind the edge for the CP800 and DP780 reamed holes. The corresponding micrograph for the CP800 reamed hole tension test acquired under the optical microscope is also shown and suggests ductile failure occurs away from the edge. The same finding was observed for in DP600 hole tension test specimens by Anderson et al. (2017) using optical microscopy. Recently, Roth and Mohr (2016) reported that the location of failure in hole tension test is dependent on the material properties and specimen geometry. The region of coalescence for the reamed samples is concentrated at the mid-plane of the sheet just away from the hole edge. Therefore, the strain localization may occur away from the edge likely due to the onset of localization which intensifies void damage. In contrast to the reamed edge model, void coalescence initiates at the sheared edge as shown in Fig. 21 for the CP800 and DP780 sheared edges. Since the maximum strain is introduced at the sheared edge, the presence of work-hardening accelerates damage accumulation and failure occurs adjacent to the sheared edge. The predicted and measured edge thickness at failure for the two steels and edge conditions are indicated in Fig. 21 and are in close agreement.

7. Conclusions

1. The work-hardening introduced behind the sheared edge promotes nucleation, growth and coalescence of voids and consequently enhances rate of damage behind the sheared edge relative to the reamed.
2. Average void growth is relatively limited during the deformation of the two steels considered; rapid increase in damage accumulation is observed close to the failure strain.
3. The histories of damage evolution and void spacing ratio as a function of equivalent strain were found to be in qualitative agreement with the predicted values for the materials and edge conditions during the hole tension test.
4. Void nucleation and coalescence primarily mainly controls ductile failure while the void growth has minor influence on the damage accumulation.
5. The micromechanics-based constitutive model proposed in the current work accurately predicts failure for the CP800 and DP780 steels for proportional loading exhibited during the reamed edge stretching as well as non-proportional loading during the sheared edge stretching during the hole tension test.

Declaration of Competing Interest

None.

Acknowledgments

Financial support for this work was provided by the Natural Sciences and Engineering Research Council of Canada (NSERC), the AUTO21 Network of Centers of Excellence, the Ontario Research Fund, and the Canada Research Chairs Secretariat. The authors would like to acknowledge the support of their industrial partner, ArcelorMittal Dofasco with special thanks to Jeff Gao and Erika Bellhouse.

Supplementary materials

Supplementary material associated with this article can be found, in the online version, at doi:10.1016/j.jmps.2019.103855.

References

Abràmoff, M., Magalhães, P., Ram, S., 2004. Image processing with Image. J. Biophoton. Int. 11 (7), 36–42.
Anderson, D., Butcher, C., Pathak, N., Worswick, M., 2017. Failure parameter identification and validation for a dual-phase 780 steel sheet. Int. J. Solids Struct. 124, 89–107.
Avramovic-Cingara, G., Ososkov, Y., Jain, M., Wilkinson, D., 2009. Effect of martensite distribution on damage behaviour in DP600 dual phase steels. Mater. Sci. Eng. A 516 (1–2), 7–12.
Bai, Y., Wierzbicki, T., 2008. A new model of metal plasticity and fracture with pressure and Lode dependence. Int. J. Plast. 24 (6), 1071–1096.
Barlat, F., Lege, D., Brem, J., 1991. A six-component yield function for anisotropic materials. Int. J. Plast. 7 (7), 693–712.
Becker, R., 1987. The effect of porosity distribution on ductile failure. J. Mech. Phys. Solids 35 (5), 577–599.
Benzerga, A., Leblond, J., 2014. Effective yield criterion accounting for microvoid coalescence. J. Appl. Mech. 81 (3), 031009.
Benzerga, A., 2002. Micromechanics of coalescence in ductile fracture. J. Mech. Phys. Solids 50 (6), 1331–1362.
Benzerga, A.A., Surovik, D., Keralavarma, S.M., 2012. On the path-dependence of the fracture locus in ductile materials – Analysis. Int. J. Plast. 37.
Butcher, C., Abedini, A., 2017. Shear confusion: identification of the appropriate equivalent strain in simple shear using the logarithmic strain measure. Int. J. Mech. Sci. 134, 273–283.
Butcher, C., 2011. A Multi-Scale Damage Percolation Model of Ductile Fracture. University of New Brunswick, Fredericton s.l.
Chu, C., Needleman, A., 1980. Void nucleation effects in biaxially stretched sheets. J. Eng. Mater. Technol. 102 (3), 249–256.
de Souza Neto, E., Peric, D., Owen, D., 2011. Computational Methods For plasticity: Theory and Applications. John Wiley & Sons: s.n.

Dykeman, J., et al., 2011. Characterization of Edge Fracture in Various Types of Advanced High Strength Steel. SAE s.l.,Technical Paper.
Gurson, 1975. Plastic Flow and Fracture Behavior of Ductile Materials, Incorporating Void Nucleation, Growth, and Interaction. Fracture Mechanics. Brown University, 1975.
Gurson, A., 1977. Continuum theory of ductile rupture by void nucleation and growth – Part I. yield criteria and flow rules for porous ductile media. J. Eng. Mater. Technol. 99, 2–15.
Huberta, C., Dubara, L., Dubara, M., Duboisa, A., 2012. Finite element simulation of the edge-trimming/cold rolling sequence: analysis of edge cracking. J. Mater. Process. Technol. 212 (5), 1049–1060.
Imbert, J.M., Winkler, S.L., Worswick, M.J., Oliveira, D.A., Golovashchenko, S., 2005. The effect of tool–sheet interaction on damage evolution in electromagnetic forming of aluminum alloy sheet. J. Eng. Mater. Technol. 127 (1), 145–153.
Kahziz, M., Morgeneyer, T.F., Mazière, M., Helfen, L., Bouaziz, O., Maire, E., 2016. In situ 3D synchrotron laminography assessment of edge fracture in dual-phase steels: quantitative and numerical analysis. Exp. Mech. 56 (2), 177–195.
Koplik, J., Needleman, A., 1988. Void growth and coalescence in porous plastic solids. Int. J. Solids Struct. 24 (8), 835–853.
Landron, C., et al., 2011. Validation of void growth models using X-ray microtomography characterization of damage in dual phase steels. Acta Mater. 59 (20), 7564–7573.
Landron, C., Bouaziz, O., Maire, E., Adrien, J., 2013. Experimental investigation of void coalescence in a dual phase steel using X-ray tomography. Acta Mater. 61 (18), 6821–6829.
Luo, M., Wierzbicki, T., 2010. Numerical failure analysis of a stretch-bending test on dual-phase steel sheets using a phenomenological fracture model. Int. J. Solids Struct. 47 (22), 3084–3102.
Nahshon, K., Hutchinson, J., 2008. Modification of the Gurson Model for shear failure. Eur. J. Mech. - A/Solids 27 (1), 1–17.
Nahshon, K., Xue, Z., 2009. A modified Gurson model and its application to punch-out experiments. Eng. Fract. Mech. 76 (8), 997–1009.
Pardoen, T., Hutchinson, J., 2000a. An extended model for void growth and coalescence. J. Mech. Phys. Solids 48 (12), 2467–2512.
Pardoen, T., Hutchinson, J., 2000b. Micromechanics-based model for trends in toughness of ductile metals. Acta Mater. 51 (1), 133–148.
Pathak, N., Adrien, J., Butcher, C., Maire, E., Worswick, M., 2019b. Experimental stress state dependent void nucleation behaviour for two 800MPa advanced high strength steels. *Submitted*.
Pathak, N., Butcher, C., Worswick, M., 2016. Assessment of the critical parameters influencing the edge stretchability of advanced high strength steel. J. Mater. Eng. Perform. 25 (11).
Pathak, N., Butcher, C., Worswick, M., 2019. Experimental techniques for finite shear strain measurement within two advanced high strength steels. Exp. Mech. 59 (2), 125–148.
Pathak, N., Butcher, C., Worswick, M., Bellhouse, E., Gao, J., 2017. Damage evolution in complex-phase and dual-phase steels during edge stretching. Materials 10 (4).
Ragab, A., 2004. Application of an extended void growth model with strain hardening and void shape evolution to ductile fracture under axisymmetric tension. Eng. Fract. Mech. 71 (11), 1515–1534.
Roth, C., Mohr, D., 2016. Ductile fracture experiments with locally proportional loading histories. Int. J. Plast. 79, 328–354.
Scheyvaerts, F., Onck, P., Tekog˘lua, C., Pardoen, T., 2011. The growth and coalescence of ellipsoidal voids in plane strain under combined shear and tension. J. Mech. Phys. Solids 59 (2), 373–397.
Thomason, C., Worswick, M., Pilkey, A., Lloyd, D., 1998. Modeling void nucleation and growth within periodic clusters of particles. J. Mech. Phys. Solids 47 (1), 1–26.
Scheyvaerts, F., Pardoen, T., Onck, P.R., 2010. A new model for void coalescence by internal necking. Int. J. Damage Mech. 19 (1), 95–126. doi:10.1177/1056789508101918, In preparation.
Thomason, P., 1999. Ductile spallation fracture and the mechanics of void growth and coalescence under shock-loading conditions. Acta Mater. 47 (13), 3633–3646.
Tvergaard, V., Needleman, A., 1984. A continuum model for void nucleation by inclusion debonding. Acta Metall. 32 (1), 157–169.
Tvergaard, V., 1981. Influence of voids on shear band instabilities under plane strain conditions. Int. J. Fract. 17 (4), 389–407.
Wang, K., Greve, L., Wierzbicki, T., 2015. FE simulation of edge fracture considering pre-damage from blanking process. Int. J. Solids Struct. 71, 206–218.
Worswick, M., Pick, R., 1990. Void growth and constitutive softening in a periodically voided solid. J. Mech. Phys. Solids 38 (5), 601–625.
Xiao, H., Bruhns, O., Meyers, A., 1997. Logarithmic strain, logarithmic spin and logarithmic rate. Acta Mech. 124 (1), 89–105.
Xue, L., 2007. Constitutive modeling of void shearing effect in ductile fracture of porous materials. Eng. Fract. Mech. 75, 3343–3366.
Zhang, L.C., et al., 2005. Nucleation of stress-induced martensites in a Ti/Mo-based alloy. J. Mater. Sci. 40 (11), 2833–2836.